In Situ Plasmonic Counter for Polymerization of Chains of Gold Nanorods in Solution

Kun Liu,[†,‡,▽,*] Aftab Ahmed,[§,▽] Siyon Chung,[‡] Kota Sugikawa,[‡] Gaoxiang Wu,[‡] Zhihong Nie,[⊥] Reuven Gordon,[§,*] and Eugenia Kumacheva[‡,∥,#,*]

[†]State Key Laboratory of Supramolecular Structure and Materials, College of Chemistry, Jilin University, Changchun 130012, P. R. China, [‡]Department of Chemistry, University of Toronto, 80 St. George Street, Toronto, Ontario M5S 3H6, Canada, [§]Department of Electrical and Computer Engineering, University of Victoria, Victoria, BC V8W 3P6, Canada, [⊥]Department of Chemistry and Biochemistry, University of Maryland, College Park, Maryland 20742, United States, [∥]Department of Chemical Engineering and Applied Chemistry, University of Toronto, 200 College Street, Toronto, Ontario M5S 3E5, Canada, and [#]The Institute of Biomaterials and Biomedical Engineering, University of Toronto, 4 Taddle Creek Road, Toronto, Ontario M5S 3G9, Canada. [▽]These authors contributed equally.

ABSTRACT Self-assembly of gold nanorods (NRs) in linear, polymer-like chains offers the ability to test and validate theoretical models of molecular polymerization. Practically, NR chains show multiple promising applications in sensing of chemical and biological species. Both areas of research can strongly benefit from the development of a quantitative tool for characterization of the structure of NR chains in the course of self-assembly, based on the change in ensemble-averaged optical properties of plasmonic polymers; however, quantitative correlation between the extinction spectra and the structural characteristics of NR chains has not been reported. Here, we report such a tool by a quantitatively correlating the red shift of the longitudinal

surface plasmon band of gold NRs and the average aggregation number of NR chains. The generality of the method is demonstrated for NRs with different aspect ratios, for varying inter-rod distances in the chains, and for varying initial concentrations of NRs in solution. We modeled the extinction spectra of the NR chains by combining the theory of step-growth polymerization with finite-difference time-domain simulations and a resistor-inductor-capacitor model, and obtained agreement between the theoretical and experimental results. In addition to capturing quantitatively the ensemble physics of the polymerization, the proposed 'plasmonic counter' approach provides a real-time cost- and labor-efficient method for the characterization of self-assembly of plasmonic polymers.
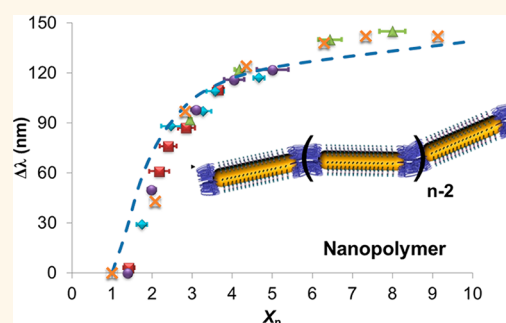
KEYWORDS: self-assembly · plasmonic polymers · gold nanorods · aggregation number · extinction spectra · simulations

S elf-assembly of nanoparticles attracts great interest for several reasons. First, in the course of self-assembly, nanoparticles act as artificial molecules, thereby offering the ability to create simple and complex model systems for their molecular analogues undergoing a chemical reaction.[1−12] For example, self-assembly of nanoparticles into small clusters, chiral structures, or polymer-like chains can be exploited to study reaction mechanisms, kinetics, and thermodynamics, as well as the formation of isomers.[13−20] This new direction of research necessitates the development of new, efficient tools for quantitative characterization of self-assembly of nanoparticles in solution.

Plasmonic nanostructures offer a very beneficial property that can be used for their structural characterization, that is, the coupling of the plasmonic properties of neighboring nanoparticles.[21−25] For polymer chains formed from plasmonic nanoparticles, the red shift in the localized surface plasmon resonance band depends on chain degree of polymerization[26,27] and offers a conceptually new strategy for polymer characterization, in comparison with conventional Gel Permeation Chromatography, Nuclear Magnetic Resonance, or viscosity techniques used for molecular polymers.[28] We stress the importance of utilization of ensemble-averaged plasmonic properties that describe the entire "reaction" system, while single particle spectroscopy provides information about each particular nanostructure but cannot be used for such a

characterization, because of the intrinsic polydispersity of the system.[12,28−30]

Second, nanoparticle assemblies often exhibit collective optical, electronic and magnetic properties that can be potentially used in nanoscale materials and devices.[31−43] In particular, self-assembled chains of gold nanorods (NRs) show extinction and surface enhanced Raman scattering (SERS) properties, which have found multiple applications in sensing of chemical and biological species.[44−50] To fully understand and utilize these properties, it is important to correlate them with structural characteristics of the NR chains.[51−53] Currently, the correlation between the average aggregation number of the chains (expressed as their number average degree of polymerization, $\bar{X}_n$) and the best sensing ability of the NR chains is not obvious. For example, our recent work shows that for a particular internanorod distance in the chains, dimers and trimers of NRs exhibit the strongest SERS enhancement.[54] *In situ* optical characterization can be efficiently used to determine the average number of NRs in the chains, after which the self-assembly process is quenched,[55] and the correlation between $\bar{X}_n$ and the optical properties of the chains is determined.

Currently, the average aggregation number of the NR chains is typically determined by analyzing their electron microscopy images.[12,54,56] A droplet of the NR solution is deposited on the grid, the solvent is removed, and the sample is imaged by collecting secondary or back-scattered electrons. Because of the low concentration of the NRs in solution, a large number of images have to be processed to obtain reliable statistical information. The process is time- and labor-consuming, and special care has to be taken to avoid artifacts, due to the drying process and the effect of the substrate. Similarly, single particle spectroscopy techniques are time-consuming, and while providing unique information about individual small clusters or plasmonic polymers,[26,57−60] cannot be used for the characterization of the collective optical properties of the entire population of chains in the system. Theoretical or numerical simulations, *e.g.*, the finite-difference time-domain (FDTD) method, the boundary element method, and the discrete dipole approximation, are also limited to a small number of objects.[61]

Currently, no optical tool addresses the questions: "How many nanorods have been assembled"? "What is the average length (or degree of polymerization) of the

chains?" or "What is the kinetics of self-assembly?" This information is buried in the extinction spectra and is important both for the applications of nanorod chains and in fundamental studies of polymerization reactions.

Here, we present a method for the quantitative characterization of the self-assembly of gold NRs in chains, which is based on the correlation between the average aggregation number of the chains and the red shift in the longitudinal surface plasmon resonance (LSPR), resulting from the surface plasmon coupling between the neighboring NRs.[62] We utilized gold NRs carrying hydrophobic polystyrene (PS) molecules at both ends, which formed chains, when the quality of the solvent for the PS tethers is reduced.[48,63] In this process, individual NRs behaved as monomers (or *nano*mers) and PS end-tethers acted as functional groups (two per each NR) (Scheme 1). In a colloidal polymer (or a *nanopolymer*), the NRs presented repeat units and the PS tethers localized between the NR ends acted as physical bonds.[64] As the NRs assembled in a nanopolymer, surface plasmon coupling between neighboring NRs resulted in red shift of the LSPR of the NRs.[62,65] The shift is determined by the length (L) and diameter (d) of individual NRs, the inter-NR distance (l), the angle (θ) between the NRs in the chains, and the number of NRs in the chain (x).

The generality of the method described in the present work was demonstrated for the NRs with different aspect ratios and for varying inter-rod distances in the chains. Importantly, in the range of NR concentrations studied, the reported correlation was independent of the initial concentration of individual NRs in the solution.

We also present the results of modeling the extinction spectra of the NR chains by combining the theory of step-growth polymerization with FDTD simulations and a resistor-inductor-capacitor (RLC) model.[66] The RLC model provides particular insight into the ensemble physics of polymer chains, whereas the FDTD simulations provide accurate solutions to the electromagnetics, specifically of the ensemble. The second model is the first quantitative description of *in situ* assembly of NPs in chains, which is important from a modeling and physics point-of-view. The theoretical predictions are in quantitative agreement with experimental results.

In addition to the time- and labor-efficient analysis of the self-assembled chains, the proposed 'plasmonic
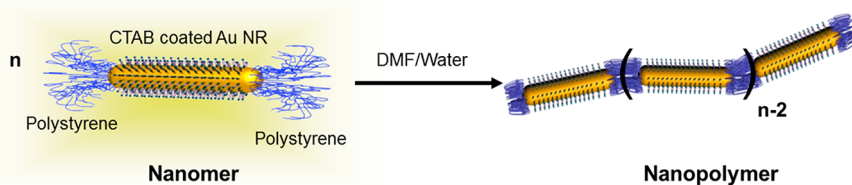
Scheme 1. Self-assembly of gold NRs end-tethered with PS functional groups in nanopolymers.

TABLE 1. The Dimensions of NRs and the Molecular Weight of the PS Ligands

samples	M_n of PS ligands	length	diameter
NR50-12k	12000	50 ± 6.1	12 ± 1.6
NR80-12k	12000	80 ± 8.7	12 ± 1.3
NR90-12k	12000	90 ± 10.4	12 ± 1.1
NR90-30k	30000	90 ± 10.4	12 ± 1.1
NR90-50k	50000	90 ± 10.4	12 ± 1.1

counter' method enables reliable *in situ* characterization of self-assembly in solution containing of up to $\sim 10^9$ plasmonic chains,[67] in comparison with $\sim 10^3$ chains characterized by image analysis. Two immediate applications of the proposed 'plasmonic counter' include (i) the capability of time- and labor-efficient examination of the kinetics of self-assembly process and (ii) studies of the correlation between the average aggregation number of the chains and their optical properties, *e.g.*, SERS enhancement factor,[54] which is important for the development of effective sensing nanostructures.

RESULTS AND DISCUSSION

Effect of Nanorod Length. Gold NRs with an average length, L, of 99 ± 10 nm and diameter, d, of 12 ± 1.8 nm were synthesized using the seed-mediated growth procedure.[68] The NRs were shortened to the average lengths of 50, 80, and 90 nm by using an etching method reported elsewhere.[69] During the etching process, the diameter of the NRs was not changed. Thiol-terminated PS molecules (M_n = 12 000 g/mol, PDI = 1.09) were selectively attached to the NR ends.[48,70] We denoted NRs with lengths of 50, 80, and 90 nm, which were tethered with PS with a molecular weight of 12 000 g/mol as NR50-12k, NR80-12k and NR90-12k, respectively (Table 1). The NRs were dispersed in dimethyl formamide (DMF). The self-assembly of the NRs in the end-to-end manner was mediated by adding water to the solution of NRs in DMF to reach the total concentration of water, C_w, of 15 wt %.[48,51] To minimize the surface energy of the system in a poor solvent, the hydrophobic PS molecules formed a physical bond between the ends of the neighboring NRs, thereby organizing NR 'nanomers' into a polymer-like chain, as shown in Scheme 1. For all the samples, the initial molar concentration of NRs in the DMF/water mixture was $[NR]_0 = 0.1 \times 10^{-9}$ mol/L.

The extinction spectra of the self-assembled NR chains were recorded in the course of NR self-assembly experiments (Figure 1). Figure 1a,b shows the variation in extinction spectra for NR50-12k and NR90-12k, respectively. While the spectral position of the transverse surface plasmon band (at 505−510 nm for both samples) remained invariant, the spectral position of the LSPR exhibited a time-dependent red-shift, characteristic of the NR association in the end-to-end

manner.[51] The change in the LSPR position, λ, was plotted as a function of the self-assembly time, t, (Figure 1c). For the NR50-12k sample, in the course of self-assembly, the shift in LSPR occurred from 836 nm ($t = 0$) to 983 nm ($t = 8$ h), and for the longer self-assembly time of up to 24 h, no further shift was observed (Figure 1a,c). For the NR80-12k sample, the shift in LSPR from 1094 to 1250 nm took a longer time of $\sim$16 h, after which the position of the peak became invariant. The LSPR peak of NR90-12k sample red-shifted from 1207 to 1390 nm in 24 h and did not reach the plateau (Figure 1b,c). These results suggested that the longer the NRs are, the larger the relative red-shift of the LSPR band is, and the longer the t is that is required to reach a plateau in the shift of LSPR.

In parallel with extinction measurements, we conducted analysis of the TEM images of the individual NRs and their chains in the self-assembling system. The inset images in Figure 1a,b show the representative TEM images of the chains of NR50-12k and NR 90-12k, respectively, formed at $t = 6$ h. Inspection of the TEM images of NR chains revealed that the average end-to-end distance between the neighboring NRs was constant during the entire self-assembly process for all the three samples. This result is consistent with the fact that all the NRs had PS end-tethers with the same molecular weight of 12 000 g/mol. The results of image analysis revealed that the number of NRs in the chains increased with the self-assembly time, t, at the expense of the decreasing number of individual NRs in the system. We characterized the average aggregation number of the NR chains, $\bar{X}_n$, by using the analogy between the NR chains and polymer chains.[12] The average aggregation number of the NR chains was determined as

$$\bar{X}_n = \frac{\text{total number of NRs}}{\text{total number of chains}} = \frac{\sum n_x x}{\sum n_x} \quad (1)$$

where x is the number of NR in the chain and n_x is the number of chains containing x NRs.[28,30]

The shift of LSPR peak, $\Delta\lambda$, was plotted *vs* $\bar{X}_n$ for the self-assembled chains of NR50-12k, NR80-12k and NR90-12k (Figure 1d). After an initial increase in $\Delta\lambda$, it reached a close-to-saturation value at $\Delta\lambda_{max}$. The variations of $\Delta\lambda$ *vs* $\bar{X}_n$ followed nearly single-exponential decay curves ($\Delta\lambda = \Delta\lambda_{max} - a\, e^{-\bar{X}_n/r}$), with decay lengths, r of 2.01 ($R^2 = 0.9934$) for NR50-12k, 2.30 ($R^2 = 0.9903$) for NR80-12k, and 2.63 ($R^2 = 0.9902$) for NR90-12k, where R^2 is the coefficient of determination. The decay length increased with the NR length. This result suggested that because a stronger plasmon coupling existed between the longer NRs, more NRs could assemble in the chain before $\Delta\lambda$ reached the saturation.

Effect of Inter-Rod Distance. We examined the correlation between $\Delta\lambda$ and $\bar{X}_n$ for the chains with different inter-rod distances, l, between adjacent NRs in the chains.
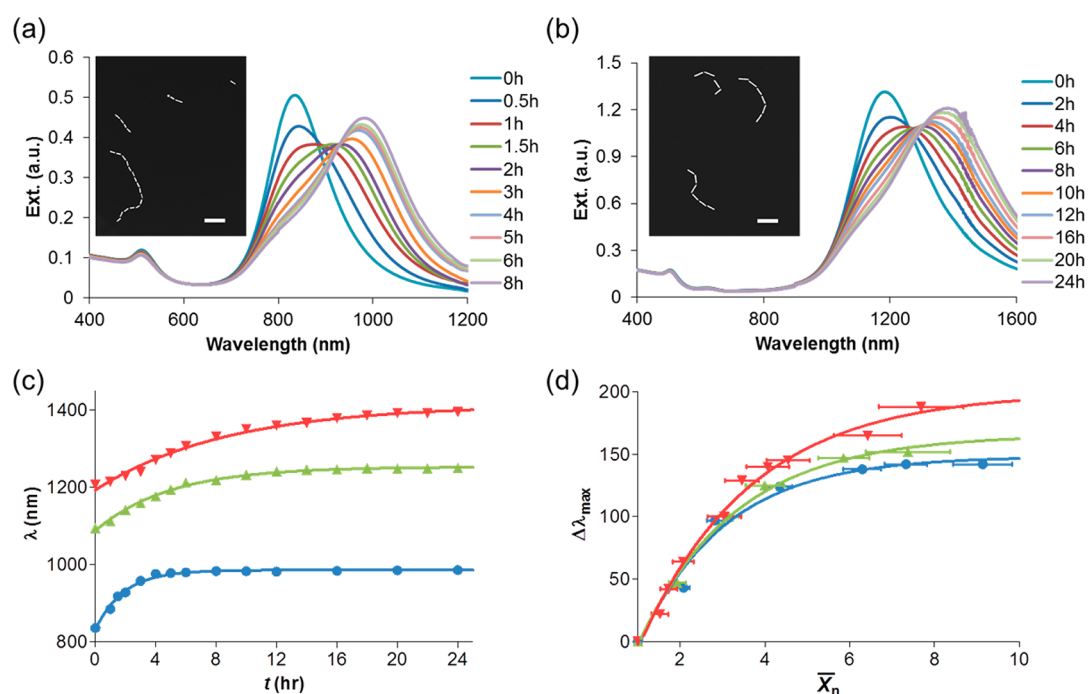
Figure 1. Variation in extinction spectra following the self-assembly of (a) NR50-12k and (b) NR90-12k. $[NR]_0 = 0.1 \times 10^{-9}$ (mol/L); $C_W = 15$ wt %. The colors of lines correspond to the different self-assembly times. The insets in (a) and (b) are the corresponding dark field TEM images of the representative NR chains at self-assembly time of 6 h. Scale bars are 200 nm. (c) Variation of LSPR peak positions (λ) with the self-assembly time, and (d) variation of the red-shift of LSPR peak positions ($\Delta\lambda$) with $\bar{X}_n$ of the NR chains for the self-assembly of NR50-12k (blue spheres), NR80-12k (green up triangles), and NR90-12k (red down triangles). The lines are exponential decay curves fitted for each sets of data points.
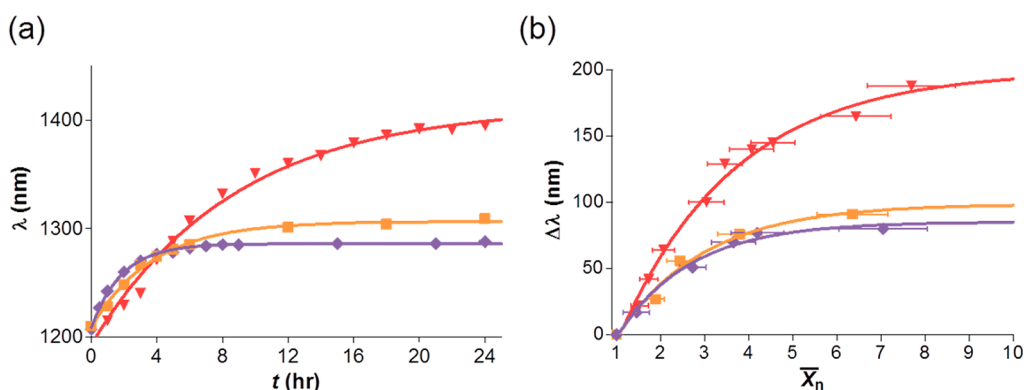

Figure 2. (a) Variation of LSPR peak positions (λ) with the self-assembly time, and (b) variation of the red-shift of LSPR peak positions ($\Delta\lambda$) with $\bar{X}_n$ of the NR chains for the self-assembly of NR90-12k (red down triangles), NR90-30k (orange squares), and NR90-50k (purple diamonds) with an initial NR concentration $[NR]_0 = 0.1 \times 10^{-9}$ (mol/L) in a DMF-water mixture at $C_w = 15$ wt %. The lines are exponential decay curves fitted for each sets of data points.

We used PS tethers with molecular weights of 12 000, 30 000 and 50 000 g/mol, which were attached to the ends of 90 nm-long NRs. The NR samples were denoted as NR90-12k, NR90-30k and NR90-50k (Table 1). The self-assembly of the NR90-12k, NR90-30k and NR90-50k samples was carried out at $[NR]_0 = 0.1 \times 10^{-9}$ (mol/L) in a DMF/water mixture at $C_W = 15$ wt %. In TEM images, the value of l was 8.2 ± 1.1, 18.3 ± 1.2, and 20.0 ± 1.9 nm for the chains formed by NR90-12k, NR90-30k, and NR90-50k, respectively. The variation in the LSPR peak position with the self-assembly time t is plotted in Figure 2a. As l increased, the shift in LSPR reached the

plateau within a shorter time, and the value of λ_{max} became smaller. Figure 2b shows the variation in $\Delta\lambda$ as a function of $\bar{X}_n$. The shift curve was fitted nearly to single-exponential decay functions with decay lengths, r, of 2.63 ($R^2 = 0.9902$) for NR90-12k, 1.96 ($R^2 = 0.9823$) for NR90-30k, and 1.67 ($R^2 = 0.9905$) for NR90-50k. The decay length decreased as the inter-rod distance increased.

Effect of Initial NR Concentration. Next, we examined whether the variation in NR concentration, $[NR]_0$, affects the relation between $\Delta\lambda$ and $\bar{X}_n$. We carried out the self-assembly in the range of concentrations of NR50-12K of $1.56 \times 10^{-10} \leq [NR]_0 \leq 5.11 \times 10^{-10}$ mol/L.
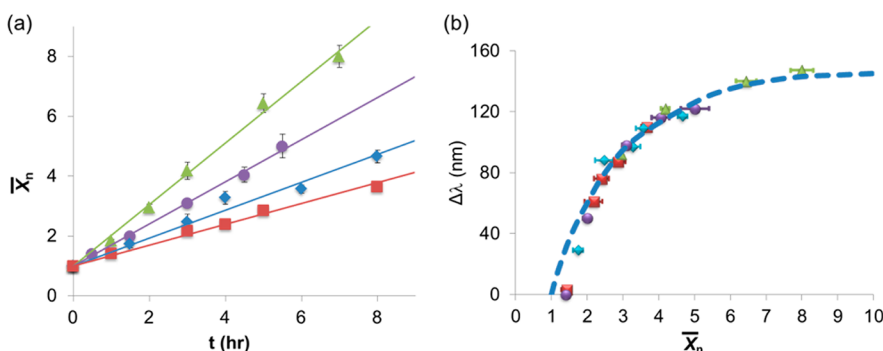
Figure 3. (a) Variation in the number average degree of polymerization, $\bar{X}_n$, of the NR chains, plotted vs self-assembly time reaction time, t, for initial concentrations of the NR50-12k of $[NR]_0 = 1.56 \times 10^{-10}$ M (red squares), $[NR]_0 = 2.42 \times 10^{-10}$ M (blue squares), $[NR]_0 = 3.51 \times 10^{-10}$ M (purple spheres) and $[NR]_0 = 5.11 \times 10^{-10}$ M (green triangles). (b) Variations of the shift of LSPR peak positions $\Delta\lambda$ with the corresponding values of $\bar{X}_n$ in (a). The blue dash line is shown for eye guidance.

The value of $[NR]_0$ was determined by measuring the intensity of extinction of the individual NRs at the wavelength corresponding to the maximum in LSPR.[34] Figure 3a shows that in the NR concentration range studied, the value of $\bar{X}$ increased linearly with t, and the higher $[NR]_0$ was, the faster $\bar{X}_n$ increased. Both features were characteristic of reaction-controlled step-growth polymerization, which was in agreement with our earlier results obtained for the assembly of arrow-headed gold NRs.[12]

Figure 3b shows the variation in $\Delta\lambda$ vs $\bar{X}_n$ at different initial NR concentrations. The relationship between $\Delta\lambda$ and $\bar{X}_n$ did not change in the entire NR concentration range. This result indicated that in a particular system, the curve of $\Delta\lambda$ vs $\bar{X}_n$ is universal, given that the NRs have identical sizes, shapes and associating ligands.

Theory of Polymerization of NRs into Linear Polymers. Gold NRs end-tethered with associating ligands form a noncovalent (physical) bond between the NR ends and undergo self-assembly in linear chains.[50] The self-assembly occurs in a stepwise manner, analogous to step-growth polymerization.[12,28,30] The first step is the reaction between two monomers to form a dimer. The dimer then forms a trimer by reacting with a monomer, or reacts with another dimer to form a tetramer. Subsequent steps include reactions between all x-mers in the system to form a nanopolymer chain, where x is the number of NRs in the chain ($x \geq 1$). The polymerization reaction yields a mixture of chains with various aggregation numbers. The number average degree of polymerization, $\bar{X}_n$, continuously increases with time as[28,30]

$$\bar{X}_n = \frac{1}{1 - p} \quad (2)$$

where p is the conversion, *i.e.* the extent of reaction

$$p = \frac{[M]_0 - [M]}{[M]_0} \quad (3)$$

where $[M]$ is the concentration of unreacted ends of NRs, and $2 \times [M]_0 = [NR]_0$.

For reaction-controlled step-growth polymerization, the concentration of chains containing x NRs, $c_{x,p}$, at conversion of p can be predicted by Flory's distribution as[28,30]

$$C_{x,p} = [NR]_0(1 - p)^2 p^{(x-1)} \quad (4)$$

where $(1 - p)^2$ is the probability of finding two unreacted functional groups at the ends of the chain, and $p^{(x-1)}$ is the probability of finding $(x - 1)$ bonds in the chain.

The normalized chain concentration $C_{x,p}/[NR]_0$ presents the number density of x-mers at conversion p. Figure S1 shows the calculated variation in $C_{x,p}/[NR]_0$ vs x, plotted for different conversion p. Although the number of individual NRs decreases as p increases, for $0 \leq p < 1$, the individual NRs (monomers) remain the most abundant species in the system. Since the ratio $C_{x+1,p}/C_{x,p} = p$, for $p < 1$, $C_{x+1,p}$ is always smaller than $C_{x,p}$.

Modeling the Extinction Spectrum of an Individual NR Chain Containing x Nanomers. The extinction spectrum of the NR chain is determined by the length, L, diameter d, of individual NRs, the inter-NR distance, l, the angle θ between the NRs, and the number x of NRs in the chain.[38] To model the spectrum of an individual NR chain, we first, assumed that the values of L, d, l and θ are constant throughout the chain and examined the relationship between x and the molar extinction coefficient, ε_x, of an individual chain with a particular, well-defined aggregation number x (increasing from 1 to 10). The end-to-end assembly of collinear NR chains was simulated by the FDTD method. The dispersive complex dielectric constant of gold was modeled using a fit to the experimental data of Johnson and Christy.[71] The simulation domain was terminated with a perfectly matched layer for minimal reflections from the boundaries. The formalism of total field scattered field was used to calculate the absorption and scattering cross sections of NR chains. The extinction cross-section was determined by the summation of scattering and absorption cross sections. For accurate modeling of the cylindrical structure in a Cartesian coordinate system,

a mesh override region was defined with a mesh size of 0.8 nm.

The extinction cross section, σ_x, obtained from FDTD simulations was converted to the molar extinction coefficient, ε_x, as $\varepsilon_x = 0.125\sigma_x N_A/(10^3 \ln 10)$, where N_A is the Avogadro's number, and the units of σ_x and ε_x are cm^2 and L mol^{-1} cm^{-1}, respectively.[72] We note that since the NRs in solution are randomly oriented with respect to the incident polarization, the factor of 0.125 accounts for NR rotation along two possible angles. The extinction can then be obtained from $Ext = \varepsilon_x bC$, where C is the concentration (in mol/L) and b is the light path length (in cm).

Figure 4 shows the results of FDTD simulations for the extinction coefficient of linear chains of NR50-12k, each containing x NRs. Figure S1 displays the normalized simulated spectra in the corresponding chains. As x increased from 1 to 10, the position of LSPR (denoted as λ) red-shifted from 836 to 976 nm. The coupling between the NRs caused the red-shift of the LSPR with increasing number of NRs in the chain. The effect was particularly strong as x increased from 1 to 5, as the majority of chain-forming NRs acquired new nearest neighbors, but then it saturated for longer chains. The normalized extinction intensity (extinction cross-section divided by x) decreased slightly as a function of x (Figure S3), which was the result of greater optical losses, as more NRs were introduced in the chains.

Modeling Extinction Spectra of the Collection of NR Chains. Next, we modeled the extinction spectra of the population of NR chains at various conversions p. For dilute colloidal solutions, the total extinction, $Ext_{tot,p}$, is the sum of extinctions of the individual species. Thus, for noninteracting self-assembled NR chains

$$Ext_{tot,p} = b(\varepsilon_1 C_{1,p} + \varepsilon_2 C_{2,p} + \varepsilon_3 C_{3,p} + ...)$$
$$= b\sum_{x=1} \varepsilon_x C_{x,p} \qquad (5)$$

where b is the light path length of a cuvette cell ($b = 1$ cm), ε_x is the extinction coefficient of the individual NR chain, $C_{x,p}$ is the mole concentration of the NR chains with a particular x at conversion p, and the subscripts 1, 2, ..., x refer to the number of NRs in the chain.

By inserting into eq 5 the values of ε_x obtained from the FDTD simulations and $c_{x,p}$ obtained from eq 4, we calculated the extinction spectra of the entire population of NR chains at various values of p (corresponding to a particular self-assembly time t). Exemplary extinction spectra for p of 0.2, 0.5, and 0.8 are shown in Figure 5a–c, respectively. The thin lines show the variation in extinction of the NR chains with a particular x, that is, $b\varepsilon_x c_{x,p}$ eq 5 where $c_{x,p}$ is calculated from eq 4 and [NR]$_0$ = 0.1 nM. The thick lines show the total extinction, $Ext_{tot,p}$, of all the chains with a particular p. For example, when $p = 0.2$, the two peaks
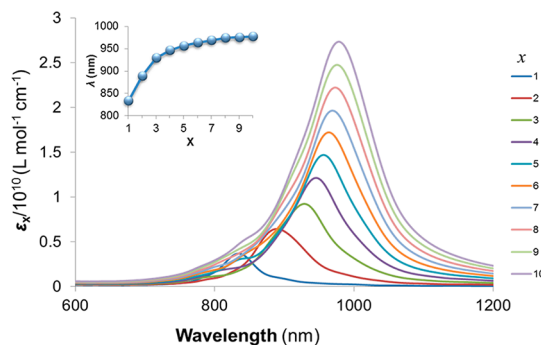

Figure 4. Simulated extinction coefficient (ε_x) of individual chains with the number of NR (x) in the chain increasing from 1 to 10. The chains are built from NR50-12K. The colors of lines correspond to the different values of x. The inset shows the variation of LSPR (λ) with x. The blue line is given for eye guidance.

at 834 and 890 nm were assigned to the individual NRs and dimers, respectively (Figure 4), and extinction of the chains with $x > 5$ was negligible. For $p = 0.5$, the extinction corresponding to monomer species significantly decreased (Figure 5b), since $C_{1,0.5} = 0.25 \times C_{1,0}$ eq 4. Extinction of NR chains with x in the range of $3 \leq x \leq 6$ increased, which led to a plateau in the spectral range from 900 to 940 nm. As the chains grew longer, the plateau shifted to longer wavelength and became the major LSPR peak at $p = 0.8$ (Figure 5c). The simulation result showed that NR chains with $1 \leq x \leq 10$ exhibited comparable extinction intensities. The summation of the extinction curves of all the x-mers yielded a total extinction curve with a LSPR peak at 978 nm.

Figure 5d shows the variation in extinction, $Ext_{tot,p}$, of the entire population of chains, calculated for $0 \leq p \leq 0.9$ by using eq 5. The intensity of LSPR at 834 nm (corresponding to the individual NRs) continuously decreased, which reflected NR consumption during the self-assembly process. Second, the total extinction in the range from 890 to 900 nm increased for $0.1 \leq p \leq 0.8$, and then gradually decreased at higher conversion. This variation corresponded to the formation of short chains with $1 < x < 6$ in the early stage of the polymerization, followed by the consumption of the short chains with the generation of longer chains ($x \geq 6$). Third, above 900 nm, extinction monotonically increased during the entire self-assembly process, which was attributed to the assembly of NR chains with $x \geq 6$ having their LSPR peaks very close to each other (Figure 4). Therefore, as the population of long chains continuously grew, the LSPR peak exhibited the increase in intensity but less red-shifting.

The simulated spectra (Figure 5d) were in a qualitative agreement with the experimental spectra (Figure 1a). The major difference between them was that the simulated spectra showed two LSPR peaks for $0.3 \leq p \leq 0.6$, while the experimental spectra showed a single peak. In addition, the experimental spectrum of
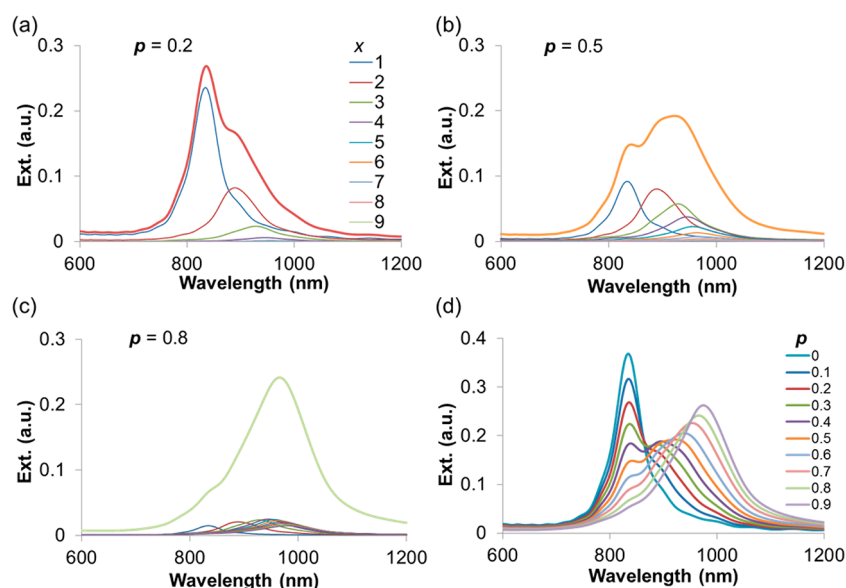
Figure 5. Simulated extinction spectra of NR chains at p of 0.2 (a), 0.5 (b), and 0.8 (c). The thin lines show extinction of the chains with each particular x showed in inset of (a), that is, $b\varepsilon_x c_{x,p}$, and the thick lines show the total extinction of the entire population of chains ($Ext_{tot,p}$). (d) Variation of $Ext_{tot,p}$ for $0 \leq p \leq 0.9$. Different colors show extinction spectra corresponding to the system at different conversions p, as in inset of (d).
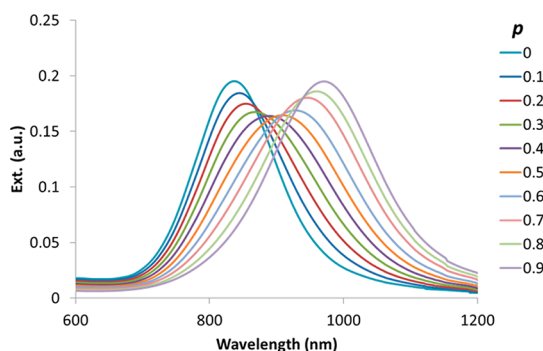

Figure 6. Simulated extinction spectra of the chains formed by polydisperse NR50-12k at different conversions, p. The different colors of the lines correspond to the different values of p (shown in inset).

Figure 7. Variation in the red-shift in LSPR ($\Delta\lambda$) with $\bar{X}_n$ for the NR chains, determined from the simulation (blue line and empty blue circles) and experimental results (solid symbols). Initial concentrations of the NRs are $[NR]_0 = 1.0 \times 10^{-10}$ M (orange crosses), $[NR]_0 = 1.6 \times 10^{-10}$ M (red squares), $[NR]_0 = 2.4 \times 10^{-10}$ M (blue squares), $[NR]_0 = 3.5 \times 10^{-10}$ M (purple spheres) and $[NR]_0 = 5.1 \times 10^{-10}$ M (green triangles).

the individual NRs exhibited a full width at half-maximum (fwhm) value of 150 nm, which was significantly broader than fwhm of ∼50 nm, obtained from FDTD simulations for monodisperse NRs with the length and diameter of 50 and 12 nm, respectively. These differences were presumably caused by the distribution of NR dimensions and the inter-NR distances in the chains (Figure S4), as well as lack of colinearity of the NRs in the chains.[55]

To account for these inhomogeneous broadenings, we used the RLC model and calculated the extinction peak position for the NR50−12K sample with the minimum and maximum aspect ratio of 3.3 and 5.2, respectively (see the histograms in Figure S4), and assuming that the NRs in the chains are colinear. The RLC model approximated a NR by a second order oscillator with damping. The overall extinction spectrum was obtained by summing the shifted and
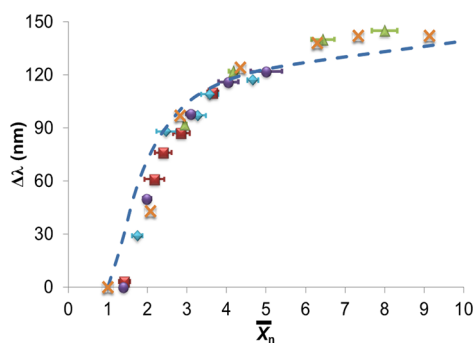
magnitude-scaled versions of the extinction spectrum corresponding to the mean dimensions.

By inserting in eq 5 the values of ε_x obtained from the RLC and FDTD simulations and $c_{x,p}$ obtained from eq 4, we calculated the extinction spectra of the entire population of NR chains formed at $0 \leq p \leq 0.9$ (Figure 6). The LSPR peak red-shifted from 836 to 976 nm, while the experimentally acquired spectra showed the corresponding shift from 836 to 978 nm. The peak intensity decreased gradually, when p increased from 0 to 0.5, reached the minimum for p at $0.4 \sim 0.5$, and then increased again. In comparison with the spectrum obtained for monodisperse NRs (Figure 5D), no multiple peaks were observed for $0.3 \leq p \leq 0.6$. The simulated spectra were in a remarkable agreement with the experimental results obtained for the NRs with the
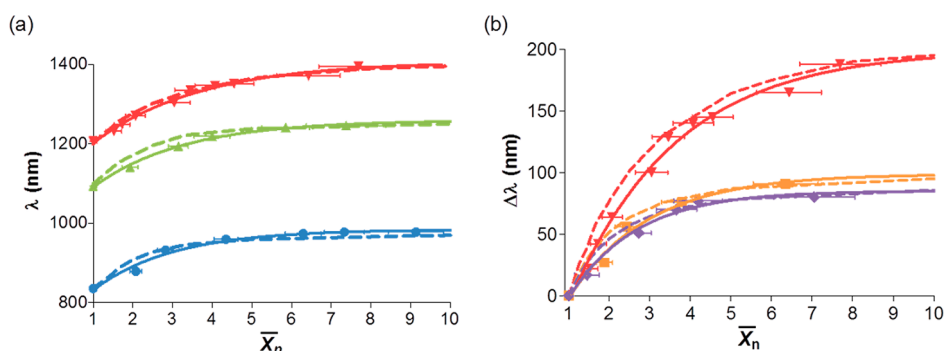
Figure 8. (a) Variations of LSPR peak positions (λ) with $\bar{X}_n$ for the NR chains for the self-assembly of NR50-12k (blue spheres), NR80-12k (green up triangles), and NR90-12k (red down triangles), and (b) variations of the red-shift of LSPR peak positions ($\Delta\lambda$) with $\bar{X}_n$ for the NR chains for the self-assembly of NR90-12k (red down triangles), NR90-30k (orange squares), and NR90-50k (purple diamonds) with an initial NR concentration $[NR]_0 = 0.1 \times 10^{-9}$ (mol/L) in a DMF-water mixture at $C_w = 15$ wt %. The lines are exponential decay curves fitted for each sets of data points. The dash lines are the corresponding curves determined from the simulation.

same length and diameter distributions. We note that the simulations showed that it takes a certain time (denoted as t_1) for the LSPR peak red-shift to reach the minimum. Based on the simulation results, at t_1 conversion p is ~0.5 ($\bar{X}_n = 2$, eq 2), that is, it takes t_1 for $\bar{X}_n$ to increase by a unit. This correlation between t_1 and $\bar{X}_n = 2$ was consistent with our previous work.[12] Finding t_1 is critical for kinetic studies of self-assembly, since the value of $\bar{X}_n$ increases linearly with the self-assembly time.

Figure 7 shows the simulated variation in the shift, $\Delta\lambda$, of LSPR (obtained from Figure 6), plotted as a function of $\bar{X}_n$ for the NR50-12K sample (the value of $\bar{X}_n$ was calculated by using eq 2). The result of the simulation showed good quantitative agreement with the experimental data.

Finally, we simulated the extinction spectra for five NR samples studied in the present work, namely, of NR50-12k, NR80-12k, NR90-12k, NR90-30k, and NR90-50k. Figure 8 shows the variation of the LSPR peak position (λ) and the variation of the red-shift of LSPR peak position ($\Delta\lambda$), both plotted as a function of $\bar{X}_n$. For all the samples, the exponential fitting curves based on the experimental results (solid lines) were in agreement with theoretical results (dashed lines). This result suggested that the theoretical model can be used to

predict the variation of the extinction spectra for the self-assembly of NR in chains, and that the shift in LSPR can be used to determine the average aggregation number of the chains.

CONCLUSION

A plasmonic counter approach enables quantitative characterization of the variation in the average aggregation number of self-assembling chains of gold NRs by measuring the shift in LSPR in extinction spectra of the system. The plasmonic counter method can be used for NRs with different lengths and associative ligands, and for varying NR concentrations in solution. We note that in the described method, the shift in LSPR is large for NR chains with low $\bar{X}_n$ and it becomes smaller for the chains with large $\bar{X}_n$. Nevertheless, because the value of $\bar{X}_n$ increases linearly with time, as long as the rate of growth of $\bar{X}_n$ is determined by using a plasmonic counter method, the value of $\bar{X}_n$ can be determined at any stage of self-assembly. We stress, however, that the method is not universal: it can be utilized for the self-assembly process that follows the kinetics of reaction-controlled step-growth polymerization, which is currently established for cylindrical and arrow-headed gold NRs.

EXPERIMENTAL SECTION

Depletion-Induced Separation of the Nanorods from Spherical Nanoparticles. As-prepared gold NRs coexisted with a small (5−10%) amount of spherical NPs with the average diameter of ~20 nm. The NPs were separated from the NRs by using depletion flocculation.[73] The solution of as-synthesized NRs at the NP concentration of 0.1 nM was heated to 60 °C and mixed with 1.65 g of hexadecyltrimethylammonium bromide (CTAB) and 2 g of benzyldimethylammonium chloride hydrate (BDAC) to increase of the concentration of CTAB from 0.055 to 0.100 M and BDAC from 0.075 to 0.125 M, respectively. The total surfactant concentration corresponded to the molar concentration of micelles of ~3.6 mM, which was 10^7 times higher than the concentration of the NRs. After adding CTAB and BDAC, the solution became opaque, due to the flocculation of long NRs. After 24 h,

the NRs settled at the bottom of the flask, the supernatant containing the NPs and the short NRs was carefully removed from the flask and deionized water was added to redisperse the settled long NRs.

Tuning Dimensions of Gold Nanorod. The NRs in an aqueous solution (1 nM, 5 mL) were etched by adding H_2O_2 solution (1M, 0.20 mL) as the method reported previously.[69] The etching process was monitored by following the shift in LSPR by using UV−vis spectroscopy. When the LSPR peak shifted to 830 nm, the NRs were removed by centrifugation.

Selective Attachment of Polystyrene Molecules to the Nanorod Ends. The aqueous solution of NRs (1.5 mL) was centrifuged twice at 10 000 rpm for 20 min to remove the supernatant. The precipitated NRs were redispersed in deionized water (30 μL). A tetrahydrofuran solution of thiol-terminated PS molecules was

prepared at polymer concentration of 0.2 mg/mL. The NR solution was rapidly injected into a 1 mL of the polymer solution and sonicated for 30 min. After sonication, the solution of NRs was incubated for 24 h at room temperature. The excess free polymer was removed from the solution by using eight centrifugation cycles, each conducted at 8500 rpm for 25 min. After each centrifugation step, the supernatant was removed and the precipitated PS-tethered NRs were redispersed in THF.

Self-Assembly of Gold Nanorods. Tetrahydrofuran was evaporated from the NR solution by using air flow. The precipitated NRs were redispersed in 0.25 g of N,N-dimethylformamide (DMF). The concentration of the NRs was determined using their absorbance at the LSPR wavelength and the corresponding molar extinction coefficients.[74] In the self-assembly experiments, it was ensured that all the NR solutions had the same initial NR concentration, $[NR]_0$ = 0.1 nM. The self-assembly process was triggered by slow, dropwise addition of 0.25 g of DMF/water mixture with the concentration of water of C_w = 30 wt % to 0.25 g of the NR solution in DMF, so that the final concentration of water in the NR solution was 15 wt %. The time at which the last drop of water−DMF mixture was added was considered as the starting time of the self-assembly (t = 0). In parallel with spectroscopic studies, the samples for TEM imaging were prepared on carbon-coated TEM grids.

Conflict of Interest: The authors declare no competing financial interest.

Supporting Information Available: Description of nanorod synthesis, distribution of NR dimensions, variation in the number density of *x*-mer nanorod chain, and experimental and simulated extinction spectra of NRs. This material is available free of charge *via* the Internet at http://pubs.acs.org.

REFERENCES AND NOTES

1. Glotzer, S. C.; Solomon, M. J. Anisotropy of Building Blocks and Their Assembly into Complex Structures. *Nat. Mater.* **2007**, *6*, 557–562.

2. Wang, Y.; Chen, G.; Yang, M.; Silber, G.; Xing, S.; Tan, L. H.; Wang, F.; Feng, Y.; Liu, X.; Li, S.; Chen, H. Systems Approach towards the Stoichiometry-Controlled Hetero-Assembly of Nanoparticles. *Nat. Commun.* **2010**, *1*, 87.

3. Maye, M. M.; Nykypanchuk, D.; Cuisinier, M.; van der Lelie, D.; Gang, O. Stepwise Surface Encoding for High-Throughput Assembly of Nanoclusters. *Nat. Mater.* **2009**, *8*, 388–391.

4. Choi, C. L.; Alivisatos, A. P. From Artificial Atoms to Nanocrystal Molecules: Preparation and Properties of More Complex Nanostructures. *Annu. Rev. Phys. Chem.* **2010**, *61*, 369–389.

5. Liao, H. G.; Cui, L.; Whitelam, S.; Zheng, H. Real-Time Imaging of Pt_3Fe Nanorod Growth in Solution. *Science* **2012**, *336*, 1011–1014.

6. Li, D.; Nielsen, M. H.; Lee, J. R.; Frandsen, C.; Banfield, J. F.; De Yoreo, J. J. Direction-Specific Interactions Control Crystal Growth by Oriented Attachment. *Science* **2012**, *336*, 1014–1018.

7. Shanbhag, S.; Tang, Z.; Kotov, N. A. Self-Organization of Te nanorods into V-Shaped Assemblies: A Brownian Dynamics Study and Experimental Insights. *ACS Nano* **2007**, *1*, 126–132.

8. Miszta, K.; de Graaf, J.; Bertoni, G.; Dorfs, D.; Brescia, R.; Marras, S.; Ceseracciu, L.; Cingolani, R.; van Roij, R.; Dijkstra, M.; Manna, L. Hierarchical Self-Assembly of Suspended Branched Colloidal Nanocrystals into Superlattice Structures. *Nat. Mater.* **2011**, *10*, 872–876.

9. Nykypanchuk, D.; Maye, M. M.; van der Lelie, D.; Gang, O. DNA-Guided Crystallization of Colloidal Nanoparticles. *Nature* **2008**, *451*, 549–552.

10. Zhang, H.; Wang, D. Controlling the Growth of Charged-Nanoparticle Chains through Interparticle Electrostatic Repulsion. *Angew. Chem., Int. Ed.* **2008**, *47*, 3984–3987.

11. Macfarlane, R. J.; Lee, B.; Jones, M. R.; Harris, N.; Schatz, G. C.; Mirkin, C. A. Nanoparticle Superlattice Engineering with DNA. *Science* **2011**, *334*, 204–208.

12. Liu, K.; Nie, Z. H.; Zhao, N. N.; Li, W.; Rubinstein, M.; Kumacheva, E. Step-Growth Polymerization of Inorganic Nanoparticles. *Science* **2010**, *329*, 197–200.

13. Wang, L. B.; Xu, L. G.; Kuang, H.; Xu, C. L.; Kotov, N. A. Dynamic Nanoparticle Assemblies. *Acc. Chem. Res.* **2012**, *45*, 1916–1926.

14. Gao, B.; Arya, G.; Tao, A. R. Self-Orienting Nanocubes for The Assembly of Plasmonic Nanojunctions. *Nature Nanotechnol.* **2012**, *7*, 433–437.

15. Abbas, A.; Kattumenu, R.; Tian, L.; Singamaneni, S. Molecular Linker-Mediated Self-Assembly of Gold Nanoparticles: Understanding and Controlling the Dynamics. *Langmuir* **2012**, *29*, 56–64.

16. Wang, H.; Chen, L.; Shen, X.; Zhu, L.; He, J.; Chen, H. Unconventional Chain-Growth Mode in the Assembly of Colloidal Gold Nanoparticles. *Angew. Chem., Int. Ed.* **2012**, *51*, 8021–8025.

17. Pyun, J. Self-Assembly and Colloidal Polymerization of Polymer−Nanoparticle Hybrids into Mesoscopic Chains. *Angew. Chem., Int. Ed.* **2012**, *51*, 12408–12409.

18. Guerrero-Martinez, A.; Auguie, B.; Alonso-Gómez, J. L.; J.; Dzolic, Z.; Gomez-Grana, S.; Zinic, M.; Magdalena C., M.; Liz-Marzan, L. M. Intense Optical Activity from Three-Dimensional Chiral Ordering of Plasmonic Nanoantennas. *Angew. Chem., Int. Ed.* **2011**, *50*, 5499–5503.

19. Guerrero-Martínez, A.; Alonso-Gómez, J. L.; Auguié, B.; Cid, M. M.; Liz-Marzán, L. M. From Individual to Collective Chirality in Metal Nanoparticles. *Nano Today* **2011**, *6*, 381–400.

20. Wang, Y.; Xu, J.; Wang, Y.; Chen, H. Emerging Chirality in Nanoscience. *Chem. Soc. Rev.* **2013**, *42*, 2930–2962.

21. Mulvaney, P. Surface Plasmon Spectroscopy of Nanosized Metal Particles. *Langmuir* **1996**, *12*, 788–800.

22. Halas, N. J.; Lal, S.; Chang, W. S.; Link, S.; Nordlander, P. Plasmons in Strongly Coupled Metallic Nanostructures. *Chem. Rev.* **2011**, *111*, 3913–3961.

23. Jones, M. R.; Osberg, K. D.; Macfarlane, R. J.; Langille, M. R.; Mirkin, C. A. Templated Techniques for the Synthesis and Assembly of Plasmonic Nanostructures. *Chem. Rev.* **2011**, *111*, 3736–3827.

24. Tan, S. J.; Campolongo, M. J.; Luo, D.; Cheng, W. Building Plasmonic Nanostructures with DNA. *Nature Nanotechnol.* **2011**, *6*, 268–276.

25. Halas, N. J.; Lal, S.; Link, S.; Chang, W. S.; Natelson, D.; Hafner, J. H.; Nordlander, P. A Plethora of Plasmonics from the Laboratory for Nanophotonics at Rice University. *Adv. Mater.* **2012**, *24*, 4842–4877.

26. Slaughter, L. S.; Willingham, B. A.; Chang, W.-S.; Chester, M. H.; Ogden, N.; Link, S. Toward Plasmonic Polymers. *Nano Lett.* **2012**, *12*, 3967–3972.

27. Barrow, S. J.; Funston, A. M.; Gómez, D. E.; Davis, T. J.; Mulvaney, P. Surface Plasmon Resonances in Strongly Coupled Gold Nanosphere Chains from Monomer to Hexamer. *Nano Lett.* **2011**, *11*, 4180–4187.

28. Odian, G. *Principles of Polymerization*, 4th ed.; Wiley: New York, 2004.

29. Slaughter, L.; Chang, W. S.; Link, S. Characterizing Plasmons in Nanoparticles and Their Assemblies with Single Particle Spectroscopy. *J. Phys. Chem. Lett.* **2011**, *2*, 2015–2023.

30. Rubinstein, M.; Colby, R. H. *Polymer Physics*; Oxford University Press: Oxford, 2003.

31. Nie, Z.; Petukhova, A.; Kumacheva, E. Properties and Emerging Applications of Self-Assembled Structures Made from Inorganic Nanoparticles. *Nat. Nanotechnol.* **2010**, *5*, 15–25.

32. Grzelczak, M.; Vermant, J.; Furst, E. M.; Liz-Marzán, L. M. Directed Self-Assembly of Nanoparticles. *ACS Nano* **2010**, *4*, 3591–3605.

33. Srivastava, S.; Kotov, N. A. Nanoparticle assembly for 1D and 2D ordered structures. *Soft Matter* **2009**, *5*, 1146–1156.

34. Fan, J. A.; Wu, C.; Bao, K.; Bao, J.; Bardhan, R.; Halas, N. J.; Manoharan, V. N.; Nordlander, P.; Shvets, G.; Capasso, F. Self-Assembled Plasmonic Nanoparticle Clusters. *Science* **2010**, *328*, 1135–1138.

35. Chang, W.-S.; Ha, J. W.; Slaughter, L. S.; Link, S. Plasmonic Nanorod Absorbers as Orientation Sensors. *Proc. Natl. Acad. Sci. U.S.A.* **2010**, *107*, 2781–2786.

36. Chang, W.-S.; Lassiter, J. B.; Swanglap, P.; Sobhani, H.; Khatua, S.; Nordlander, P.; Halas, N. J.; Link, S. A Plasmonic Fano Switch. *Nano Lett.* **2012**, *12*, 4977–4982.

37. Liu, N.; Mukherjee, S.; Bao, K.; Li, Y.; Brown, L. V.; Nordlander, P.; Halas, N. J. Manipulating Magnetic Plasmon Propagation in Metallic Nanocluster Networks. *ACS Nano* **2012**, *6*, 5482–5488.

38. Sánchez-Iglesias, A.; Grzelczak, M.; Altantzis, T.; Goris, B.; Pérez-Juste, J.; Bals, S.; Van Tendeloo, G.; Donaldson, S. H.; Chmelka, B. F.; Israelachvili, J. N.; Liz-Marzán, L. M. Hydrophobic Interactions Modulate Self-Assembly of Nanoparticles. *ACS Nano* **2012**, *6*, 11059–11065.

39. Fang, Y.; Chang, W.-S.; Willingham, B.; Swanglap, P.; Dominguez-Medina, S.; Link, S. Plasmon Emission Quantum Yield of Single Gold Nanorods as a Function of Aspect Ratio. *ACS Nano* **2012**, *6*, 7177–7184.

40. Lattuada, M.; Hatton, T. A. Synthesis, Properties and Applications of Janus Nanoparticles. *Nano Today* **2011**, *6*, 286–308.

41. Lee, G.; Cho, Y. S.; Park, S.; Yi, G. R. Synthesis and Assembly of Anisotropic Nanoparticles. *Korean J. Chem. Eng.* **2011**, *28*, 1641–1650.

42. Gao, Y.; Tang, Z. Y. Design and Application of Inorganic Nanoparticle Superstructures: Current Status and Future challenges. *Small* **2011**, *7*, 2133–2146.

43. Zhang, H.; Liu, Y.; Yao, D.; Yang, B. Hybridization of Inorganic Nanoparticles and Polymers to Create Regular and Reversible Self-Assembly Architectures. *Chem. Soc. Rev.* **2012**, *41*, 6066–6088.

44. Wang, L. B.; Zhu, Y. Y.; Xu, L. G.; Chen, W.; Kuang, H.; Liu, L. Q.; Agarwal, A.; Xu, C. L.; Kotov, N. A. Side-by-Side and End-to-End Gold Nanorod Assemblies for Environmental Toxin Sensing. *Angew. Chem., Int. Ed.* **2010**, *49*, 5472–5475.

45. Chen, H.; Shao, L.; Li, Q.; Wang, J. Gold Nanorods and Their Plasmonic Properties. *Chem. Soc. Rev.* **2013**, *42*, 2679–2724.

46. Alvarez-Puebla, R. A.; Agarwal, A.; Manna, P.; Khanal, B. P.; Aldeanueva-Potel, P.; Carbó-Argibay, E.; Pazos-Pérez, N.; Vigderman, L.; Zubarev, E. R.; Kotov, N. A.; Liz-Marzán, L. M. Gold Nanorods 3D-Supercrystals as Surface Enhanced Raman Scattering Spectroscopy Substrates for the Rapid Detection of Scrambled Prions. *Proc. Natl. Acad. Sci. U.S.A.* **2011**, *108*, 8157–8161.

47. Sudeep, P. K.; Joseph, S. T. S.; Thomas, K. G. Selective Detection of Cysteine and Glutathione Using Gold Nanorods. *J. Am. Chem. Soc.* **2005**, *127*, 6516–6517.

48. Nie, Z. H.; Fava, D.; Kumacheva, E.; Zou, S.; Walker, G. C.; Rubinstein, M. Self-Assembly of Metal-Polymer Analogues of Amphiphilic Triblock Copolymers. *Nat. Mater.* **2007**, *6*, 609–614.

49. Chen, T.; Wang, H.; Chen, G.; Wang, Y.; Feng, Y.; Teo, W. S.; Wu, T.; Chen, H. Hotspot-Induced Transformation of Surface-Enhanced Raman Scattering Fingerprints. *ACS Nano* **2010**, *4*, 3087–3094.

50. Liu, K.; Zhao, N.; Kumacheva, E. Self-Assembly of Inorganic Nanorods. *Chem. Soc. Rev.* **2011**, *40*, 656–671.

51. Nie, Z. H.; Fava, D.; Rubinstein, M.; Kumacheva, E. "Supramolecular" Assembly of Gold Nanorods End-Terminated with Polymer "Pom-Poms": Effect of Pom-Pom Structure on the Association Modes. *J. Am. Chem. Soc.* **2008**, *130*, 3683–3689.

52. Zhu, Z.; Liu, W.; Li, Z.; Han, B.; Zhou, Y.; Gao, Y.; Tang, Z. Manipulation of Collective Optical Activity in One-Dimensional Plasmonic Assembly. *ACS Nano* **2012**, *6*, 2326–2332.

53. Grzelczak, M.; Mezzasalma, S. A.; Ni, W.; Herasimenka, Y.; Feruglio, L.; Montini, T.; Pérez-Juste, J.; Fornasiero, P.; Prato, M.; Liz-Marzán, L. M. Antibonding Plasmon Modes in Colloidal Gold Nanorod Clusters. *Langmuir* **2011**, 8826–8833.

54. Lee, A.; Andrade, G. F. S.; Ahmed, A.; Souza, M. L.; Coombs, N.; Tumarkin, E.; Liu, K.; Gordon, R.; Brolo, A. G.; Kumacheva, E. Probing Dynamic Generation of Hot-Spots in Self-Assembled Chains of Gold Nanorods by Surface-Enhanced Raman Scattering. *J. Am. Chem. Soc.* **2011**, *133*, 7563–7570.

55. Chen, G.; Wang, Y.; Tan, L. H.; Yang, M.; Tan, L. S.; Chen, Y.; Chen, H. High-purity Separation of Gold Nanoparticle Dimers and Trimers. *J. Am. Chem. Soc.* **2009**, *131*, 4218–4219.

56. Joseph, S. T. S.; Ipe, B. I.; Pramod, P.; Thomas, K. G. Gold Nanorods to Nanochains: Mechanistic Investigations on Their Longitudinal Assembly Using α,ω-Alkanedithiols and Interplasmon Coupling. *J. Phy. Chem. B* **2006**, *110*, 150–157.

57. Funston, A. M.; Novo, C.; Davis, T. J.; Mulvaney, P. Plasmon Coupling of Gold Nanorods at Short Distances and in Different Geometries. *Nano Lett.* **2009**, *9*, 1651–1658.

58. Tabor, C.; Van Haute, D.; El-Sayed, M. A. Effect of Orientation on Plasmonic Coupling between Gold Nanorod. *ACS Nano* **2009**, *3*, 3670–3678.

59. Shao, L.; Woo, K. C.; Chen, H.; Jin, Z.; Wang, J.; Lin, H.-Q. Angle- and Energy-Resolved Plasmon Coupling in Gold Nanorod Dimers. *ACS Nano* **2010**, *4*, 3053–3062.

60. Slaughter, L. S.; Wu, Y.; Willingham, B. A.; Nordlander, P.; Link, S. Effects of Symmetry Breaking and Conductive Contact on the Plasmon Coupling in Gold Nanorod Dimers. *ACS Nano* **2010**, *4*, 4657–4666.

61. Myroshnychenko, V.; Rodriguez-Fernandez, J.; Pastoriza-Santos, I.; Funston, A. M.; Novo, C.; Mulvaney, P.; Liz-Marzan, L. M.; Abajo, F. J. G. D. Modeling the Optical Response of Gold Nanoparticles. *Chem. Soc. Rev.* **2008**, *37*, 1792–1805.

62. Jain, P. K.; Eustis, S.; El-Sayed, M. A. Plasmon Coupling in Nanorod Assemblies: Optical Absorption, Discrete Dipole Approximation Simulation, and Exciton-Coupling Model. *J. Phys. Chem. B* **2006**, *110*, 18243–18253.

63. Fava, D.; Nie, Z. H.; Winnik, M. A.; Kumacheva, E. Evolution of Self-Assembled Structures of Polymer-Terminated Gold Nanorods in Selective Solvents. *Adv. Mater.* **2008**, *20*, 4318–4322.

64. Lukach, A.; Liu, K.; Therien-Aubin, H.; Kumacheva, E. Controlling the Degree of Polymerization, Bond Lengths, and Bond Angles of Plasmonic Polymers. *J. Am. Chem. Soc.* **2012**, *134*, 18853–18859.

65. Sun, Z. H.; Ni, W. H.; Yang, Z.; Kou, X. S.; Li, L.; Wang, J. F. pH-Controlled Reversible Assembly and Disassembly of Gold Nanorods. *Small* **2008**, *4*, 1287–1292.

66. Huang, C.-P.; Yin, X.-G.; Kong, L.-B.; Zhu, Y.-Y. Interactions of Nanorod Particles in the Strong Coupling Regime. *J. Phys. Chem. C* **2010**, *114*, 21123–21131.

67. In a typical NR solution, the concentration of NRs is on the order of ∼0.1 nM and the solution volume is ∼1 mL. The number of NRs is thus 0.1 pM, which is corresponds to the 10^{10} of NRs. The average aggregation number of ∼10 corresponds to 10^9 chains.

68. Nikoobakht, B.; El-Sayed, M. A. Preparation and Growth Mechanism of Gold Nanorods (NRs) Using Seed-Mediated Growth Method. *Chem. Mater.* **2003**, *15*, 1957–1962.

69. Ni, W.; Kou, X.; Yang, Z.; Wang, J. Tailoring Longitudinal Surface Plasmon Wavelengths, Scattering and Absorption Cross Sections of Gold Nanorods. *ACS Nano* **2008**, *2*, 677–686.

70. Petukhova, A.; Greener, J.; Liu, K.; Nykypanchuk, D.; Nicolay, R.; Matyjaszewski, K.; Kumacheva, E. Standing Arrays of Gold Nanorods End-Tethered with Polymer Ligands. *Small* **2012**, *8*, 731–737.

71. Johnson, P. B.; Christy, R. W. Optical Constants of the Noble Metals. *Phys. Rev. B* **1972**, *6*, 4370–4379.

72. Lakowicz, J. R. *Principles of Fluorescence Spectroscopy*, 3rd ed.; Springer: New York, 2006, p 59.

73. Park, K.; Koerner, H.; Vaia, R. A. Depletion-Induced Shape and Size Selection of Gold Nanoparticles. *Nano Lett.* **2010**, *10*, 1433–1439.

74. Orendorff, C. J.; Murphy, C. J. Quantification of Metal Content in the Silver-Assisted Growth of Gold Nanorods. *J. Phys. Chem. B* **2006**, *110*, 3990–3994.